Boosting the Electrocatalytic Activity of Co_3O_4 Nanosheets for Li-O_2 Battery through Modulating Inner Oxygen Vacancy and Exterior Co^{3+}/Co^{2+} Ratio

Junkai Wang [a‖], Rui Gao [a‖], Dong Zhou [b], Zhongjun Chen [c], Zhonghua Wu [c], Gerhard Schumacher[b], Zhongbo Hu[a] and Xiangfeng Liu [a*]

[a] College of Materials Science and Opto-Electronic Technology, University of Chinese Academy of Sciences, Beijing 100049, P. R. China.

[b] Helmholtz-Center Berlin for Materials and Energy, Hahn-Meitner-Platz 1, 14109 Berlin, Germany

[c] Beijing Synchrotron Radiation Facility, Institute of High Energy Physics, Chinese Academy of Sciences, Beijing 100049, China

‖ **These two authors contributed equally to this work.**

*Corresponding Author: liuxf@ucas.ac.cn

TOC

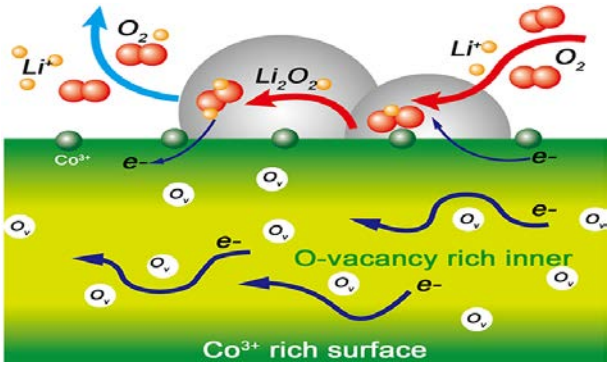
O2
Li+
Li2O2
Li+
O2
Co3+
e-
e-
e-
e-
e-
O-vacancy rich inner
Co3+ rich surface

Abstract

Rechargeable Li-O_2 batteries have been considered as the most promising chemical power owing to their ultrahigh specific energy density. But the sluggish oxygen reduction reaction (ORR) and oxygen evolution reaction (OER) result in the high overpotential (~1.5V), the poor rate capability and even the short cycle life, which critically hinder their practical applications. Herein, we propose a synergistic strategy to boost the electrocatalytic activity of Co_3O_4 nanosheets for Li-O_2 battery by tuning the inner oxygen vacancies and the exterior Co^{3+}/Co^{2+} ratio which have been identified by Raman spectroscopy, X-ray photoelectron spectroscopy and X-ray Absorption Near Edge Structure spectroscopy. *Operando* X-ray diffraction and *ex-situ* Scanning Electron Microscope are used to probe the evolution of the discharge product. In comparison with bulk Co_3O_4, the cells catalyzed by Co_3O_4 nanosheets show a much higher initial capacity (~24051.2mAh g^{-1}), better rate capability (8683.3mAh g^{-1}@400mA g^{-1}) and cycling stability (150 cycles@400mA g^{-1}), and lower overpotential. The large enhancement of the electrochemical performances can be greatly attributed to the synergistic effect of the architectured 2D nanosheets, the oxygen vacancies and Co^{3+}/Co^{2+} difference between the surface and the interior. Moreover, the addition of LiI in the electrolyte can further reduce the overpotential making the battery more practical. This study offers some insights into designing high performance electrocatalysts for Li-O_2 batteries through the combination of the 2D nanosheets architecture, oxygen vacancy and surface electronic structure regulation.

KEYWORDS: Co_3O_4 nanosheets; oxygen vacancy; surface electronic modulation; synergetic effect; Li−O_2 battery

Introduction

In recent years, some new electrochemical power sources such as Li-S, Zn-air, Al-air and Li-air batteries have been intensively explored in order to alleviate the energy crisis and environmental issue resulting from the overuse of fossil fuels.[1-5] In comparison with Li-S, Zn-air, Al-air or Li-ion batteries, Li-air battery shows a much higher specific energy (~3600Wh kg^{-1}) and attracts great interest.[5-7] However, the sluggish kinetics of the oxygen reduction reaction (ORR) and oxygen evolution reaction (OER) on the cathode, and the resultant large overpotential, low energy efficiency, the inferior rate performance and the poor cycle life have critically impeded their practical applications in electric vehicles (EVs).

In order to overcome the above problems some strategies including the design of bifunctional cathode catalysts, the electrolyte mediation, and the regulation of the discharge product morphology or composition have been extensively explored.[8-11] Some previous studies have shown that the use of some suitable catalysts is one of the effective ways to reduce the overpotential of Li-air cells and extend the cycle life.[12-13] Noble metals (Au, Pt, Pd etc.) have shown excellent performance but the price is too high. Some carbon materials exhibit a high ORR activity but their OER performance is usually inferior, and they are also easy to be oxidized inducing some side reactions at a high voltage. On the contrary, transition metal oxides (MnO_2, Co_3O_4, $NiCo_2O_4$, etc.) have attracted great interest due to their low cost and high efficiency.[14-18] The OER activity of metal oxides is usually higher than that of carbon materials. It has

been well accepted that the OER process is more important in improving the reversible capability and cycle life during the electrochemical process. As for the metal oxide catalysts, the surface atom arrangement or valance distribution plays a significant role on the elecrocatalytic activity and the electrochemical performances of Li-O_2 battery, and some strategies (i.e. crystal plane, doping, vacancy engineering) have also been taken to tune the surface atom or electronic structure. [19-21] Our group and some other groups have reported the crystal plane dependence of the electrocatalytic activity of Co_3O_4 for Li-O_2 battery.[12-13, 22] Tuning the electronic structure to increase active sites through creating oxygen vacancies is another effective strategy to enhance the electrocatalytic activity of metal oxide catalysts for Li-O_2 cells.[23-25] Chen et al. improved the ORR activity of MnO_2 through generation of oxygen vacancies.[25] Recently, 2D nanosheets based on transition metal oxides have also attracted great attention as efficient electrocatalysts.[26-29] In addition, another study also indicates that the surface atoms with lowered coordination number can act as active sites for adsorption of O_2.[29] However, the design and large-scale synthesis of noble metal free cathode catalysts with both high ORR and OER reactivity is still a big challenge for the development and application of lithium-air battery.

Herein, we propose a synergistic strategy to enhance the electrocatalytic activity of Co_3O_4 nanosheets as cathode catalyst for Li-O_2 battery by tuning the inner oxygen vacancy concentration and the exterior Co^{3+}/Co^{2+} ratio. Compared to bulk Co_3O_4, the cells catalyzed by the Co_3O_4 nanosheets show a much higher initial capacity, better rate capability and cycling stability, and lower overpotential, which can be greatly attributed to the synergistic effect of the architectured 2D nanosheets, the

inner oxygen vacancies and the Co^{3+}/Co^{2+} difference between the surface and theinterior. Moreover, the addition of LiI into the electrolyte can further reduce the overpotential and improve the electrochemical performances of Li-O_2 batteries.[30]

Experimental Methods

Co_3O_4 ultrathin nanosheets were prepared by a two-step method which include the synthesis of precursor and sintering under O_2:

Hydrothermal synthesis of $Co(CO_3)_{0.5}(OH) \cdot 0.11H_2O$ precursor: We synthesized $Co(CO_3)_{0.5}(OH) \cdot 0.11H_2O$ precursor by hydrothermal method. In a typical process, 300mg $Co(acac)_3$(III) and 1.1g cetyltrimethyl ammonium bromide (CTAB) were first dissolved into the mixture of 5.5ml deionized water and 30 ml EG (Ethylene glycol) to form a homogeneous suspension by magnetic stirring and ultrasonic. Then, the suspension was transferred into 50 ml Teflon-lined autoclave and maintained at 180 °C for 48 h. After cooling down to ambient temperature, the final product was collected by rapid vacuum filtration with washing by ethanol and water for many times. Then dried in vacuum overnight for further characterization.

Sintering synthesis of nanosheets: The as-obtained $Co(CO_3)_{0.5}(OH) \cdot 0.11H_2O$ precursor was directly calcined at 320 °C for 5 minutes in pure O_2 and then cooled down to room temperature. Finally, the obtained powders were collected for further characterization.

Materials characterization

All the samples were characterized by X-ray diffraction (XRD) in a RIGAKU SMARTLAB diffractometer with a Cu-K□ radiation source. Data were collected in the range of 10–80° at a scan rate of 10° min^{-1}. Operando X-ray diffraction patterns were collected on Li−O_2 battery on 4B9A Beamline of BSRF with Mythen Detector.[31-32] The data was collected every 20 min when discharging at a current density of 200mA g^{-1}. [33]

The morphological studies of the samples and the cathodes were performed on a HITACHI SU8010 scanning electron microscope (SEM) and a transmission electron microscope (TEM HITACHI HT7700 excellent).

X-ray photoelectron spectroscopy (XPS) was measured on a Thermo escalab 250Xi with a monochromatic X-ray source (E (Al Kα) = 1486.6 eV). Each spectrum was normalized using the regain of C 1s (284.6 eV) as the line position of adventitious carbon.

Soft XAS measurements were performed at Russian-German Beamline of the synchrotron Bessy II, Berlin, Germany. Data were obtained both in total electron yield (TEY) and fluorescence yield (TFY) modes at room temperature under ultrahigh vacuum (10^{-9} Torr). The emitted total number of electrons from the sample were counted in TEY mode and the energy dispersive Bruker XFlash® fluorescence detector was used in FY mode.

Raman spectra were obtained from the RENISHEW inVia confocal Raman microscope with an excitation wavelength of 532 nm ranging from 200cm^{-1} to 1000cm^{-1}.

Nitrogen sorption isotherms were measured at 77 K using a Micromeritics ASAP-2020 analyzer. Before measurements, the samples were degassed in a vacuum at 200 °C for 4 h. The surface area of the powder was calculated by the Brunauer–Emmett–Teller (BET) method.

Electrochemical measurements

The electrochemical performance of the Li–O_2 cell was analyzed using a 2025-type coin cell. The cathode and the cells were assembled as follows: 40 wt% Co_3O_4 catalyst, 20 wt% polyvinylidene fluoride (PVDF) and 40 wt% super P carbon were mixed with N-methyl-2-pyrrolidone to prepare a catalyst slurry. The mixture was then dispersed on the carbon paper current collector to prepare the porous air electrode, which was then dried at 120 °C under vacuum for 12 h. The loading of the active materials (Co_3O_4 and super P) is about 1.33mg cm^{-2}. All the specific capacity and discharge/charge current density were calculated based on the mass of Co_3O_4 and Super P. All the cells were assembled in a glovebox under an Ar atmosphere with oxygen and water contents less than 0.1 ppm, using a lithium metal foil anode, a glass fibre separator, an oxygen cathode and an electrolyte containing 1 M LiTFSI in TEGDME. The galvanostatic charge and discharge performance of the batteries was tested on a LAND CT2001A battery test system with the voltage between 2.0 and 4.5

V at room temperature. The galvanostatic discharge/charge tests were performed in a specific capacity-controlled mode (500 mAh g^{-1}) at a current density of 400 mA g^{-1}. Various current densities (100, 200, 500) were tested to investigate the rate capability of the prepared samples. The electrochemical impedance spectra (EIS) and cyclic voltammetry (CV) measurements were performed on PRINCETON PMC-2000 electrochemical workstation. All the electrochemical tests were performed at pure oxygen atmosphere.

Results and discussion

Co_3O_4 nanosheets (Co_3O_4-NS) were synthesized by sintering in an oxygen atmosphere. Figure 1a show the XRD patterns of Co_3O_4 nanosheets and commercial bulk Co_3O_4. All the diffraction peaks of the two samples can be well indexed to standard PDF card of a pure spinel Co_3O_4 phases (PDF No.43-1003). Compared with Co_3O_4 bulks, some characteristic peaks of the Co_3O_4 nanosheets become broaden and the peak of (111) is strengthened. The results demonstrate a preferential orientation of (111).[21] Figure 1b shows the curves of Raman spectra of Co_3O_4 nanosheets and bulk Co_3O_4. Four characteristic peaks in the curve located at 471, 513, 608 and 677 cm^{-1} can be indexed to Raman active modes of the crystal Co_3O_4 corresponding to E_g, F^1_{2g}, F^2_{2g} and A_{1g}.[34-35] The left shift and broadening of the peaks in Co_3O_4-NS indicate that the crystallization degree has become weakened and the surface electronic structure statement has changed after calcination in oxygen. [22]

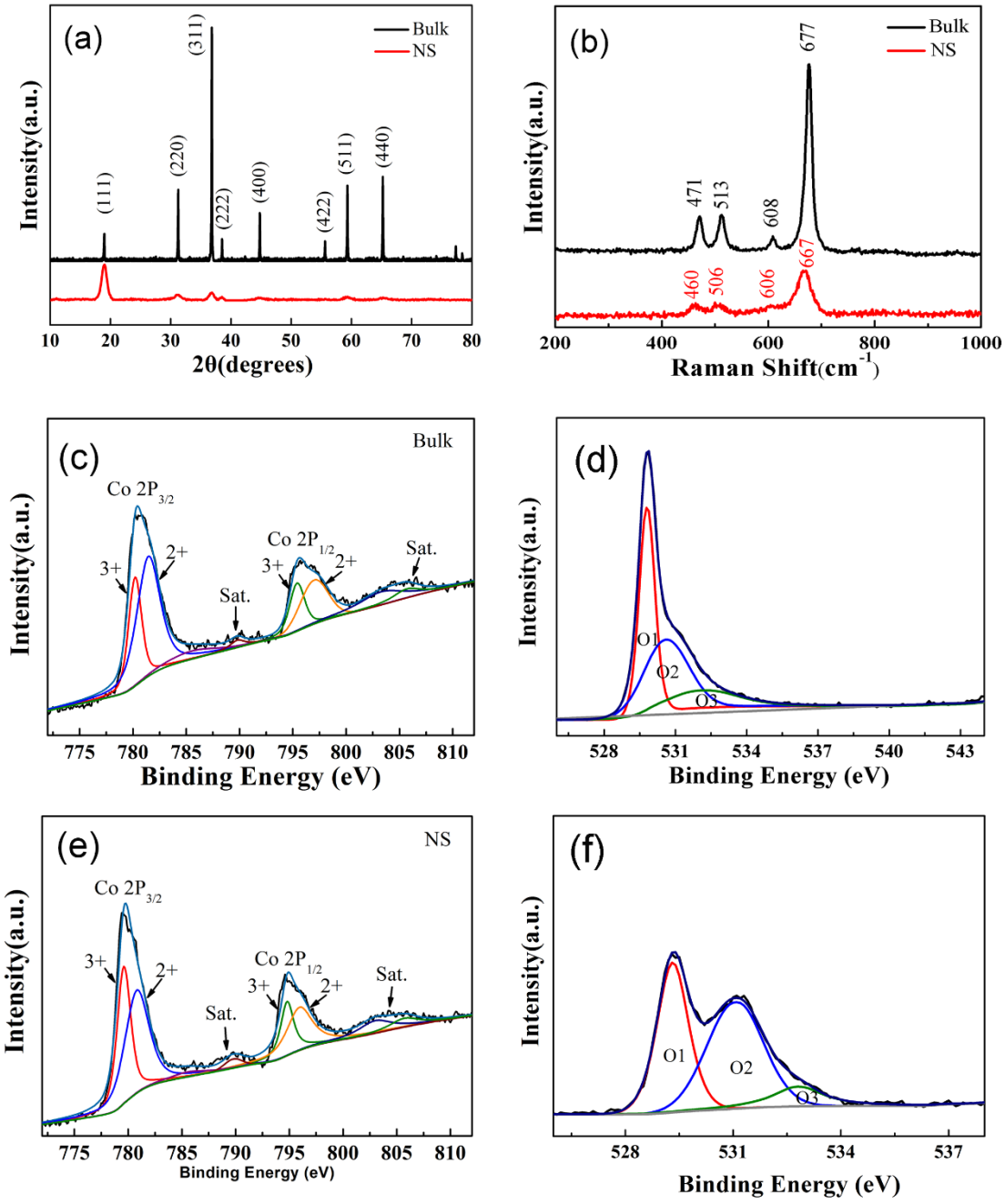

Figure 1. (a, b) XRD patterns and Raman spectra of the Co_3O_4 nanosheet (NS) and Co_3O_4 bulk (Bulk); (c) XPS spectra of Co 2p for Co_3O_4 bulk; (d) XPS spectra of O 1s for Co_3O_4 bulk; (e) XPS spectra of Co 2p for Co_3O_4 nanosheet; (f) XPS spectra of O 1s for Co_3O_4 nanosheet.

X-ray photoelectron spectroscopy (XPS) have been used to analyze the electronic structure and surface oxidation states of Co_3O_4 nanosheets. In the core level spectra of Co 2p region, the two samples show two major peaks with binding energy of 779.5 eV and 794.7 eV as shown in Figure1c, e. The main peak can be fitted by two regions of Co^{3+} and Co^{2+}.[36-37] By comparing the ratio of Co^{3+}/Co^{2+} of the two different Co_3O_4 samples, it can be concluded that the Co^{3+}/Co^{2+} ratio (0.75) of NS-Co_3O_4 is higher than that of bulk Co_3O_4 (0.48), which means more Co^{3+} are exposed on the surface of Co_3O_4 nanosheets. In the O 1s core level spectra, we can clearly identify three peaks. In detail, the peaks at 529.8 eV, 531 eV and 532.6 eV can be ascribed to metal-oxide, defect sites and hydroxyl species respectively.[38-39] Figure1d and f show the O2 peak, and the species is obviously strengthened in NS-Co_3O_4. This can be ascribed to a higher concentration of vacancies in the nanosheets compared with the bulk, which is in well agreement with the results shown in the Raman spectrum. Both of two measurements confirm that the surface atom state of Co_3O_4 nanosheets is different from that of bulk Co_3O_4. On the other hand, nanosheets have larger specific surface area (56 m^2g^{-1}) than bulk specimens (24 m^2g^{-1}) indicating that the nanosheets can supply more active sites. Figure S1 shows N_2 adsorption-desorption isotherms for Co_3O_4 nanosheet (NS) and Co_3O_4 bulk (Bulk).

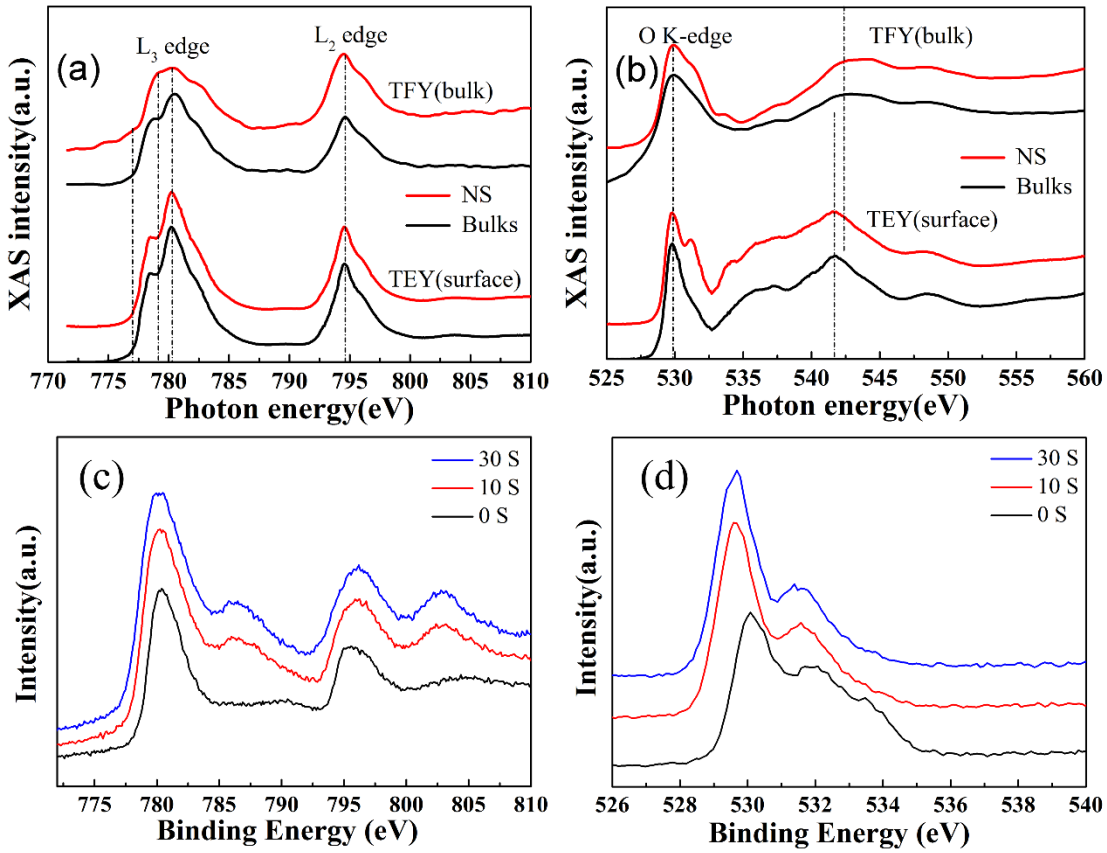

Figure 2. (a) Co L2,3-edge XANES spectra measured in TFY and TEY mode, and (b) The O K-edge XANES spectra; (c) XPS spectra of O1s for Co_3O_4 bulk specimens before and after etching; (d) XPS spectra of O 1s for Co_3O_4 nanosheets before and after etching.

In order to find out more detailed information about the electronic structure of the nanosheets on the surface and in the bulk, the X-ray Absorption Near Edge Structure (XANES) spectroscopy was employed, since the XANES data can be recorded simultaneously in both total electron yield mode (TEY) and fluorescence yield mode (TFY) with different probing depth.[40-41] Total electron yield mode probes the surface information with a depth ~ 5nm, while the data collected in the fluorescence yield mode provides the information from the bulk with a probing depth

of ~ 50 nm. Normalized XANES at Co L-edge and O K-edge are shown in Figure 2a and 2b, respectively. As can be seen from Figure 2a, the peaks at about 780eV and 795eV could be assigned to the L_3-edge and L_2-edge of Co^{3+} in a low spin state. While the peak of the Co_3O_4 nanosheets at 779 eV measured in TFY mode indicates the presence of Co^{2+} in bulk. This demonstrates that the Co ions of the nanosheets cannot be oxidized to Co^{3+} completely, but only part of Co^{2+} on the surface ions are oxidized. However, in the interior, Co^{2+} act as the dormitory role. As shown in Figure 2b, the O K-edge XANES spectra of Co_3O_4 nanosheet and bulk specimens have a few distinct features in the range from 529 eV to 550 eV, at both TEY and TFY modes. The peak at 529.8 eV can be attributed to the bond of Co 3d/O2p.[42-44] The difference in the degree of oxygen adsorption in the interior and at the surface of the NS causes some offset of the peak position at ~ 542.5eV, which was finally confirmed by the XPS analysis of the samples with different etching time (Figure 2d). In Figure 2d, the bond energy and peak shape of O 1s has changed obviously, while all three peaks of O1s in Figure 2c are similar. After refreshing the surface by the etching for several seconds, the location of O1s bonding energy of Co_3O_4 nanosheets become quite different. The shift of the peak to lower energy as a function of etching time reflects the weakening of the Co-O bond. Thus, it is reasonable to conclude that a large number of oxygen vacancies exist in the interior and more Co^{3+} ions form on the outer surface of Co_3O_4 nanosheets.

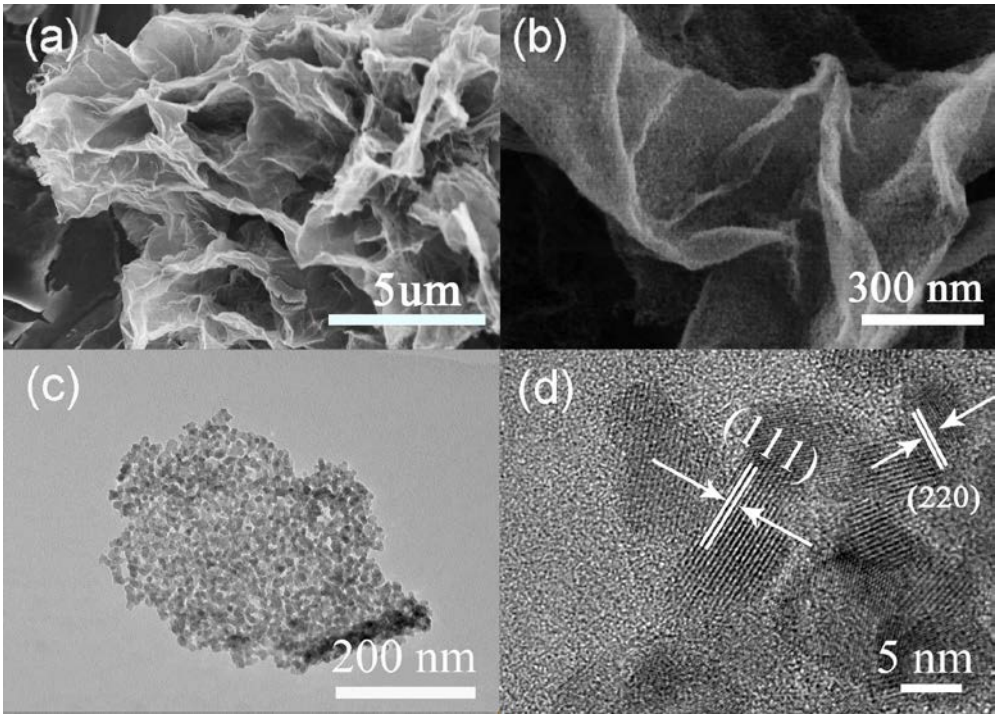

Figure 3. (a, b) SEM images of the nanosheets at different magnifications viewed from the top; (c) TEM image of a NS specimen viewed from the top; (d) High-resolution TEM micrograph of a Co_3O_4 NS specimen.

The morphology can be observed by field-emission scanning electron microscope (FE-SEM) and transmission electron microscope (TEM) as shown in Figure 3. The Co_3O_4 nanosheets reveal a thickness of a few nanometers and a size of 300-500 nm. Figure 3d shows a high-resolution transmission electron microscopy (HRTEM) micrograph of a Co_3O_4 nanosheet. The images collected at the edge of the Co_3O_4 nanosheets reveal lattice fringes of 0.467 nm and 0.286 nm, respectively, indicating the (111) and (220) planes. It can be observed that this Co_3O_4 nanosheet is not a complete structure, but contain a large number of pores with sizes ranging from 2-4 nm, in Figure 3c. This will make the surface area increase largely. Hence,

according to the 2D morphological structure, directional crystal growth and special surface state can improve the catalytic performance and the electrochemical properties of the Li-O_2 battery.

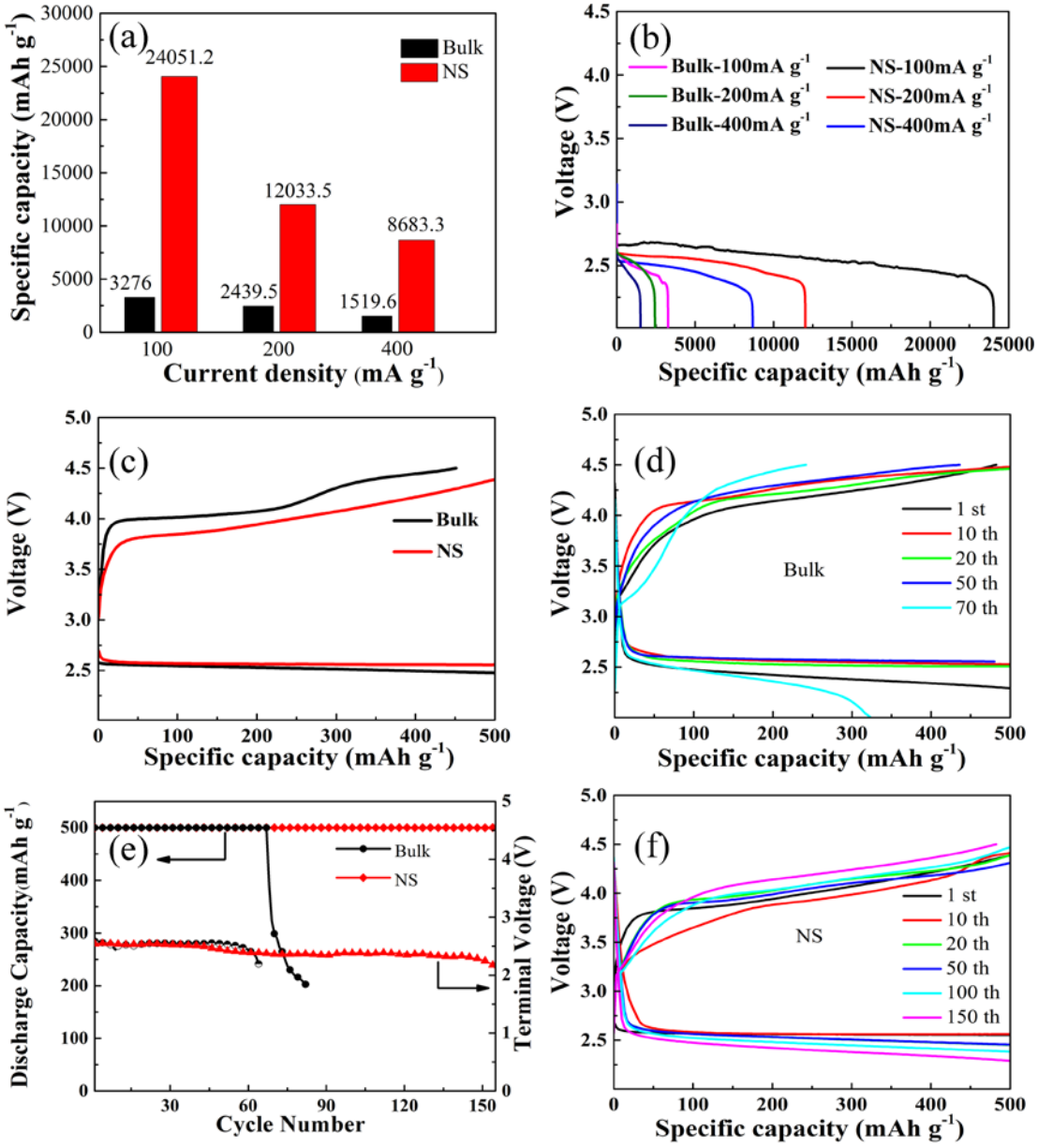

Figure 4. Specific capacity at 100, 200 and 400 mA g^{-1}, respectively, for the bulk and nanosheet sample(a) bar graph; (b) Voltage versus specific capacity curve; (c) Comparison of the first limited discharge–charge curves for nanosheet and bulk

specimens, measured at a current density of 400 mA g^{-1}; (d, f) The discharge curves at different cycles of Co_3O_4 bulks and Co_3O_4 nanosheets; (e) The cycle performance and terminal voltage of two samples based cathodes when the capacity is limited to 500 mAh g^{-1} at a current density of 400 mA g^{-1}.

As shown in Figure 4a and b, the electrochemical performances for Co_3O_4 bulk and nanosheets were tested at different current density of 100, 200 and 400 mA g^{-1}. The initial discharge capacity of nanosheets is significantly higher than that of bulk specimens when assembled as Li-O_2 coin cell. In terms of specific capacity, the discharge specific capacity of Co_3O_4 bulk is 3276.3mAh g^{-1}, 2439.5mAh g^{-1} and 1519.6mAh g^{-1}, respectively. But the discharge specific capacity of nanosheets is largely increased to 24051.2mAh g^{-1}, 12033.5mAh g^{-1} and 8683.3mAh g^{-1}, respectively. With the increase in current density, the charge potential increases and the discharge potential reduces. In Figure 4d, f, as the number of the cycles increases, the overpotential of the two samples increases. However, the battery catalyzed by bulk Co_3O_4 cannot get a long-term cycle. After 60 cycles, the capacity cannot reach 500mAh/g. Figure 4c shows the first discharge-charge curves of cathodes at 400 mA g^{-1} based on bulks and nanosheets. The terminal discharge voltage of Co_3O_4 bulk is about 2.6 V (vs Li^+/Li) with a terminal charge voltage close to 4.24 V (vs Li+/Li). After several cycles, the cell catalyzed by bulks cannot be completely charged. However, the nanosheet based cathodes show a lower overpotential and better reversibility, which indicates nanosheets have a higher OER activity. In Figure 4e, with a capacity limitation of 500 mAh g^{-1} and current densities of 400 mA g^{-1}, the

Co_3O_4 bulk electrode can run 66 cycles, while the nanosheets can last 156 cycles. After 56 cycles, the discharge voltage of the bulk specimens is drastically reduced. In contrast, after 156 cycles, the discharge terminal voltage of the NS specimens remains at about 2.2V. The nanosheets demonstrate a largely enhanced cycling performance. The coulomb efficiency curves for Co_3O_4 nanosheet (NS) and Co_3O_4 bulk (Bulk) are shown in Figure S2, which can obviously explain the ORR and OER performance of these two materials. After 40 cycles, the coulombic efficiency of Co_3O_4 bulk based battery decreases, while the Co_3O_4 nanosheets based battery can be well maintained until 120 cycles.

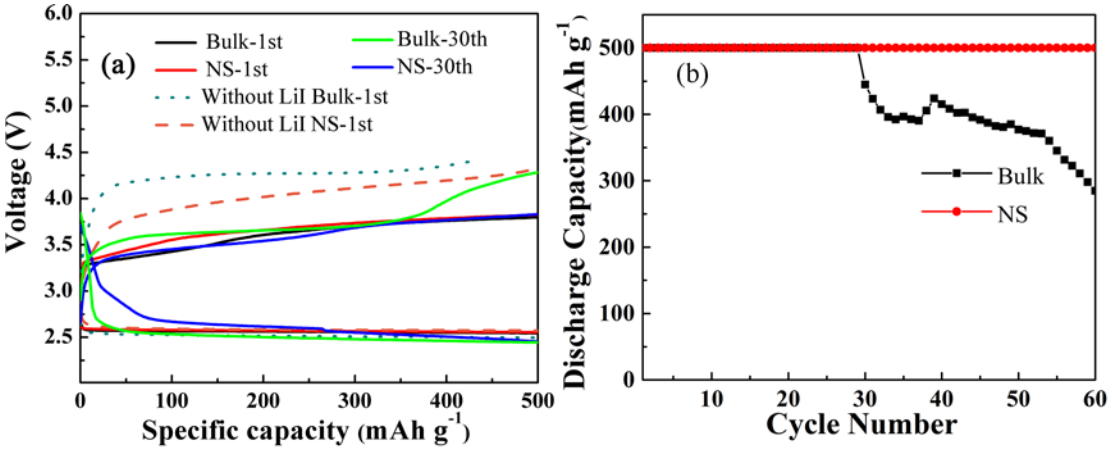

Figure 5. The electrochemical performances of Co_3O_4 nanosheets and Co_3O_4 bulks based Li-O_2 battery with LiI additives in the electrolyte at a current density of 200 mA g^{-1}. (a) The discharge–charge curves at 1st and 30th of Co_3O_4 nanosheets and Co_3O_4 bulks. (b) The cycle performance of specimens with NS and bulk based cathodes with LiI in the electrolyte.

It is reported that the additive LiI can significantly reduce the overpotential.[45-47] Therefore, LiI was applied to further enhance the performance of the whole cell. As

shown in Figure 5a, the initial charging potential of Co_3O_4 nanosheets and Co_3O_4 bulks based Li-O_2 battery with LiI additives has been lowered to about 3.5V. After 30 cycles, the charge potential of bulk Co_3O_4 based battery increases considerably and the discharge platform is reduced due to the insufficient catalytic activity, which results in a larger overpotential. In contrary, the charge and discharge platform of the nanosheets-catalyzed Li-O_2 cell remains very stable after 30 cycles indicating the Co_3O_4 nanosheets have a much higher catalytic activity. In addition, in the electrolyte containing LiI additive, the cycle performance of the battery using the nanosheets is still much better than that of bulks, which means the addition of LiI additive and the use of the nanosheets catalyst can cooperatively reduce the overpotential and enhance the electrochemical performance of Li-O_2 battery.

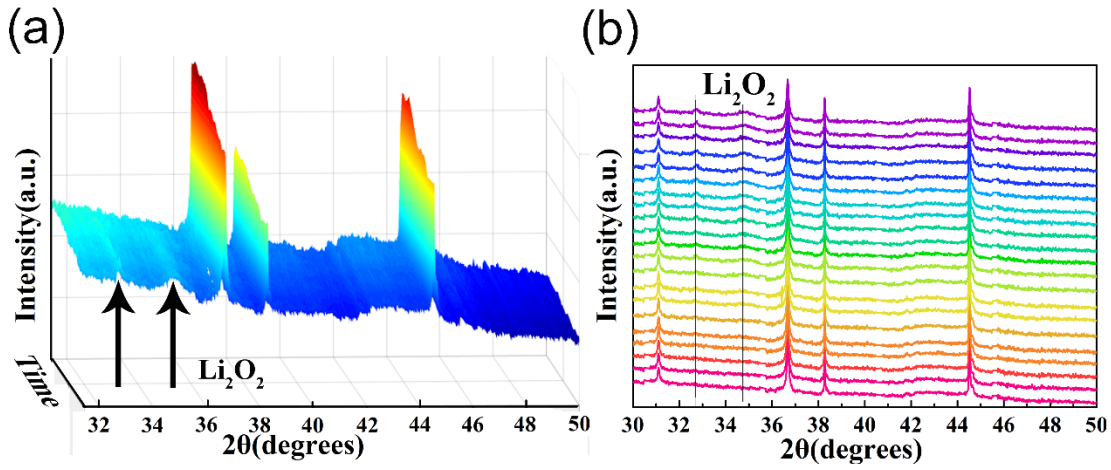

Figure 6. (a) Three dimensional discharge plots of the XRD patterns in the 2θ region of 30−50°, with a constant current of 200 mA g^{-1}, (b) 2D image of the in-situ XRD.

In order to explain the products and the corresponding potential in the process of discharging, *operando* XRD of the electrode was obtained with different time, as

shown in Figure 6. In the discharge process, the peak of catalyst Co_3O_4 is obviously located at 2θ = 31.3°, 36.9° and 44.9°, and the peaks at 32.6° and 34.8° can be indexed as the lattice planes of (200) and (201), respectively, of Li_2O_2. As the discharge goes on, the peaks became obvious, which indicates the formation of discharge product Li_2O_2. In Figure 6, the peaks at 32.6° and 34.8° appeared simultaneously, which may display that the growth of Li_2O_2 is not directional. After 2 hours, the obvious peak can be detected on the pattern. In order to further explain the discharge mechanism and the distribution of the product, the morphology of the electrodes (Co_3O_4 bulk and nanosheets) at different discharge state (0, 500, 1000mAh g^{-1}) are investigated as shown in Figure 7. Before discharge, the Co_3O_4 bulk and nanosheet mixed with Super P can be clearly observed on the pristine cathodes in Figure 7a and c, respectively. Accumulation of catalyst can be seen in local area. After a small discharge of 500mAh g^{-1}, lamellar Li_2O_2 has formed and Co_3O_4 bulk structure became blurry. In contrast, the thickness of Li_2O_2 is smaller in nanosheet based electrode. Finally, after discharge of 1000 mAh g^{-1}, the products of the crystalline platelet-shape Li_2O_2 were full of vision. The result well agreed with the XRD patterns: Li_2O_2 first formed as an amorphous film and then grew into nanosheets resulting in broadened diffraction peaks; as the discharge continues, the discharge products crystallized into platelet shape with an obvious diffraction peak. We used XRD and SEM to characterize the decomposition of the discharge product Li_2O_2 on the Co_3O_4 nanosheets based electrode after recharging to 1000 mAh g^{-1} as shown in Figure S3 and S4. Figure S3 shows the XRD pattern of the Co_3O_4 nanosheets based

electrode after recharge to 1000 mAh g^{-1}. As shown in Figure S3, no detectable diffraction peaks of Li_2O_2 were found in the pattern, which means the Li_2O_2 decomposes completely after recharging. Figure S4 shows the SEM image of the Co_3O_4 nanosheets based electrode after recharge to 1000 mAh g^{-1}. As shown in Figure S4, the platelet-shape Li_2O_2 disappears after recharge which further indicates that Li_2O_2 decomposes completely after recharge to 1000 mAh g^{-1}.

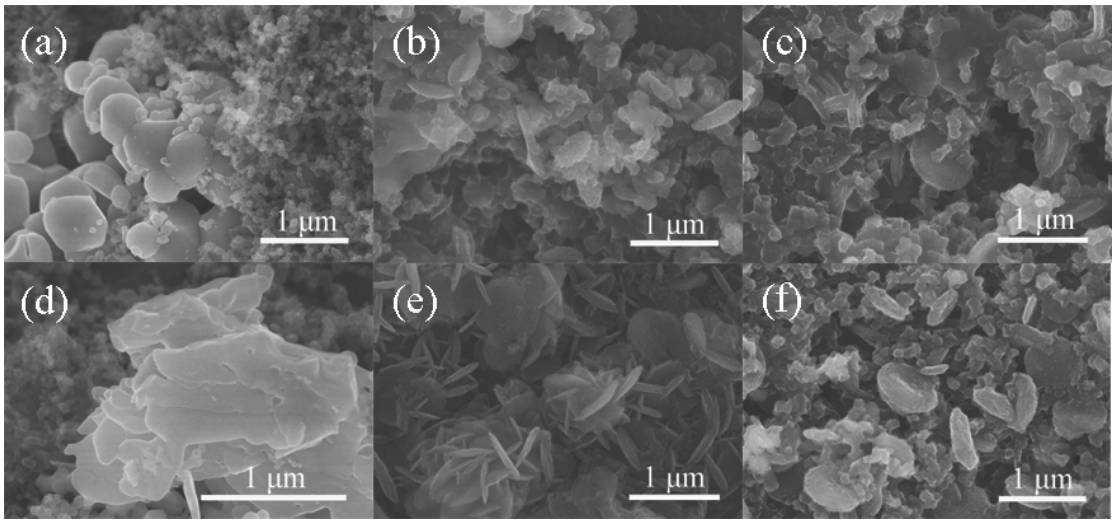

Figure 7. SEM images of Co_3O_4 bulks and Co_3O_4 nanosheets electrodes after discharge to (a, d) 0 mAh g^{-1}; (b, e) 500 mAh g^{-1}; (c, f) 1000mAh g^{-1}, respectively.

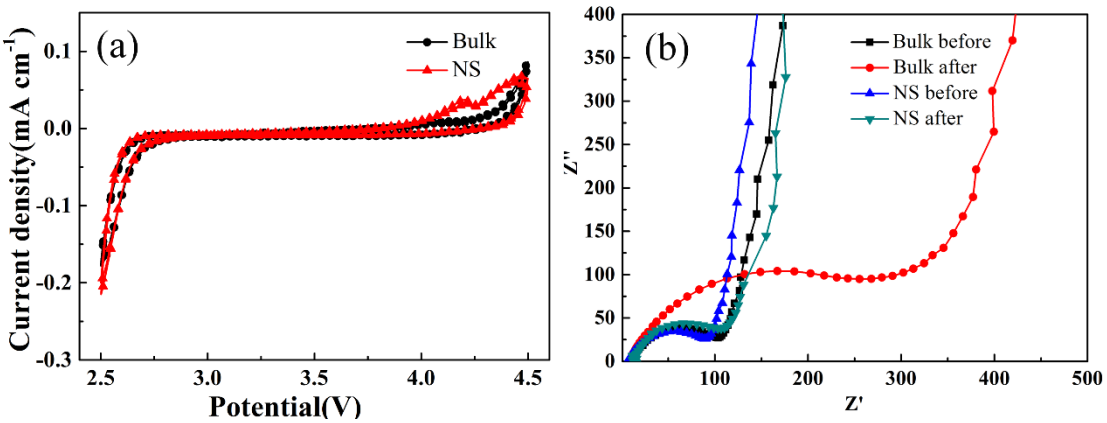

Figure 8. (a) CV curves in the LiTFSI/TEGDME electrolyte at a scan rate of 0.1 mV

s^{-1}; (b) Electrochemical impedance spectra (EIS) of nanosheets and bulks of discharged/recharged cathodes.

ORR and OER performance of nanosheets and bulk were also examined in 2025-type Li-O_2 coin cell in pure O_2 environment. As the shown in Figure 8a, nanosheets and bulk shows the same ORR activity between 3.0V to 2.5V. However, during the OER process at above 4.0V, the CV curve of the battery catalyzed by Co_3O_4 NS shows classical redox behavior,[48] with two oxidation peaks at 4.0~4.25 and 4.25~4.5V. It means Co_3O_4-NS can obviously enhance the OER process for the Li-O_2 battery. We further verified the superior electrochemical performances of nanosheets by electrochemical impedance spectroscopy (EIS). We measured the EIS of the two samples. Before the recharging, the charge transfer resistance (R_{ct}) of the nanosheets and bulks is very close (~100Ω) as shown in Figure 8b. After several cycles, the R_{ct} of bulk specimen based Li-O_2 battery becomes extremely large. The main reason is that more discharge product accumulates on the cathode of Co_3O_4 bulk due to the weak OER performance, which may affect the conductivity of the cell and increase Rct. The nanosheets have better cycle performance, in terms of impedance recovery, and the nanosheets are an effective catalyst for reversible electrochemical processes. All these results illustrate that Co_3O_4 nanosheets exhibit the better electrochemical performance which is not only because of large surface area, but, more importantly, result from the difference of the surface state of Co atom within the NS and outside the NS. In this material, Co^{3+} on the surface are the main active sites for ORR and OER. While more Co^{2+} within the material can also coordinate to enhance the

performance of the nanosheets. On the other hand, the oxygen vacancies in the interior of Co_3O_4 nanosheets accelerate the electron and Li^+ conductivity as well as accelerate OER process.[49]

The large enhancement of the electrochemical performances can be greatly attributed to the synergistic effect of the architectured 2D nanosheets, the rich oxygen vacancies in the inner and the Co^{3+}/Co^{2+} difference between the surface and the interior as shown in Figure 9. Figure 9 presents a schematic illustration of the synergetic effect of the architectured 2D nanosheets, the inner rich oxygen vacancies and the rich Co^{3+} on the surface. The large specific surface area of 2D materials is favorable to be full contact and infiltration with the electrolyte and oxygen.[50] The oxygen vacancies in the interior facilitate the electron and Li^+ conductivity as well as accelerate OER process as active sites binding to O_2 and Li_2O_2.[51] The nanosheets have more Co^{3+} on the surface and more Co^{2+} in the inner. Similar to spinel λ-MnO_2, the Co^{2+}/Co^{3+} redox reaction can react with superoxide and Li_2O_2 to promote the ORR and OER reaction during the cycles. The Co^{3+} on the surface catalyzes both OER and ORR reactions, and the discharge product Li_2O_2 forms and decomposes on the surface. The difference of Co^{3+}/Co^{2+} ratio between the surface and the interior will further enhance the conductivity and the electrocatalytic activity of Co_3O_4.

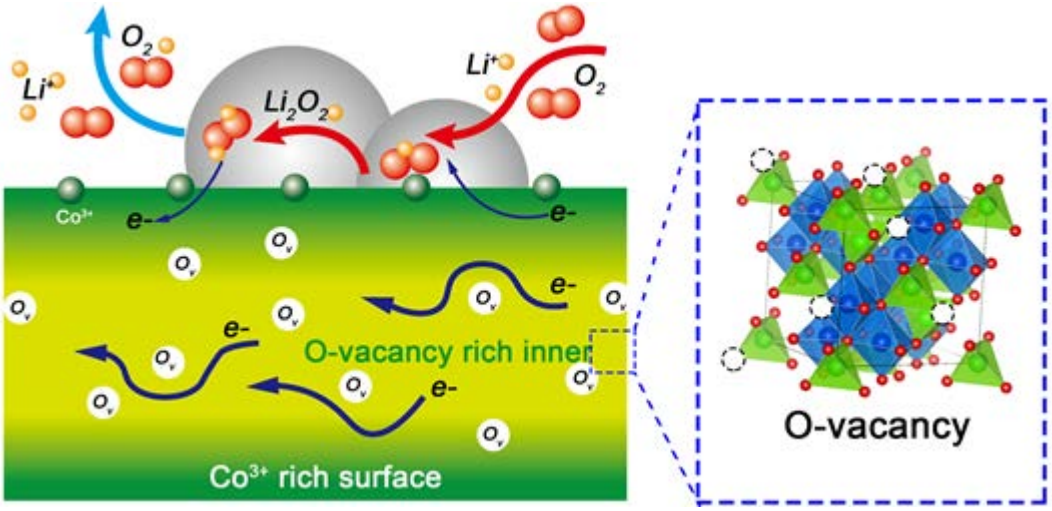

Figure 9. Schematic illustration of the synergetic effect of the architectured 2D nanosheets, with high concentration of oxygen vacancies in the interior and high Co^{3+} concentration on the surface.

Conclusion

The high electrocatalytic activity of Co_3O_4 nanosheets for Li-O_2 battery has been achieved by tuning the concentration of inner oxygen vacancies and the Co^{3+}/Co^{2+} ratio at the surface. In comparison to bulk Co_3O_4, the cells catalyzed by Co_3O_4 nanosheets show a much higher initial capacity, better rate capability and cycling stability, and lower overpotential, which can be greatly attributed to the synergistic effect of the architectured 2D nanosheets, the oxygen vacancies and Co^{3+}/Co^{2+} difference between the surface and the interior. In addition, the overpotential can be further reduced and the electrochemical performances of Li-O_2 batteries can be further improved by adding LiI in the electrolyte which makes Li-O_2 battery more practical. This study offers some new insights into designing high performance

electrocatalysts for Li-O_2 batteries through tuning 2D nanosheets architecture, oxygen vacancy and surface electronic structure.

ASSOCIATED CONTENT

Supporting Information. N_2 adsorption-desorption isotherms and coulomb efficiency curves for Co_3O_4 nanosheet (NS) and Co_3O_4 bulk (Bulk); XRD and SEM of the Co_3O_4 nanosheets based electrode after recharge to 1000 mAh g^{-1}. This material is available free of charge via the Internet at http://pubs.acs.org.

AUTHOR INFORMATION

Corresponding Author

*E-mail: liuxf@ucas.ac.cn. Tel.: +86 10 8825 6840.

Acknowledgements

This work was supported by National Natural Science Foundation of China (Grant 11575192), the State Key Project of Fundamental Research (Grant 2014CB931900) of Ministry of Science and Technology of the People's Republic of China, the Scientific Instrument Developing Project and “Hundred Talents Project” of the Chinese Academy of Sciences. Allocation of beamtime at RGBL beamline, BESSY-II, Berlin, Germany, is gratefully acknowledged.

References:

(1) Thotiyl. M. M. O.; Freunberger, S. A.; Peng, Z.; Chen, Y.; Liu, Z.; Bruce, P. G. *Nat. Mater.* **2013,** *12*, 1050-1056.

(2) N. Feng, P. He, H. Zhou, *Adv. Energy Mater.* **2016**, *6*, 1502303.

(3) Débart, A.; Paterson, A. J.; Bao, J.; Bruce, P. G. *Angew.Chem. Int. Ed.* **2008,** *47*, 4521-4524.

(4) Black, R.; Adams, B.; Nazar, L. F. *Adv. Energy Mater.* **2012**, *2*, 801-815.

(5) Bruce, P. G.; Freunberger, S. A.; Hardwick, L. J.; Tarascon, J. M. *Nat. Mater.* **2012,** *11*, 19-29.

(6) Geng, D.; Ding, N.; Hor, T. S. A.; Chien, S. W.; Liu, Z.; Wu, D.; Sun, X.; Zong, Y. *Adv. Energy Mater.* **2016,** *6*, 1502164.

(7) Grande, L.; Paillard, E.; Hassoun, J.; Park, J. B.; Lee, Y. J.; Sun, Y. K.; Passerini, S.; Scrosati, B. *Adv. Mater.* **2015,** *27*, 784-800.

(8) Ma, R.; Sasaki, T. *Adv. Mater.* **2010,** *22*, 5082-5104.

(9) Liu, Y.; Xiao, C.; Li, Z.; Xie, Y. *Adv. Energy Mater.* **2016**, 6, 1600436.

(10) Lim, H. D.; Lee, B.; Zheng, Y.; Hong, J.; Kim, J.; Gwon, H.; Ko, Y.; Lee, M.; Cho, K.; Kang, K. *Nat. Energy* **2016,** *1*, 16066.

(11) Cheng, F.; Zhang, T.; Zhang, Y.; Du, J.; Han, X.; Chen, J. *Angew.Chem. Int. Ed.* **2013,** *52*, 2474-2477.

(12) Gao, R.; Liu, L.; Hu, Z.; Zhang, P.; Cao, X.; Wang, B.; Liu, X. *J Mater. Chem. A* **2015,** *3*, 17598-17605.

(13) Gao, R.; Zhu, J.; Xiao, X.; Hu, Z.; Liu, J.; Liu, X. *J. Phys. Chem. C* **2015,** *119*, 4516−4523.

(14) Cao, X.; Wu, J.; Jin, C.; Tian, J.; Strasser, P.; Yang, R. *ACS Catal.* **2015,** *5*, 4890-4896.

(15) Lin, X.; Lv, X.; Wang, L.; Zhang, F.; Duan, L. *Mater. Res. Bull.* **2013,** *48*, 2511-2516.

(16) Xia, H.; Zhu, D.; Luo, Z.; Yu, Y.; Shi, X.; Yuan, G.; Xie, J. *Sci. Rep.* **2013,** *3*, 2978.

(17) Shen, C.; Wen, Z.; Wang, F.; Wu, X.; Chen, C. *JOM* **2016,** *68*, 2585-2592.

(18) Yang, L. C.; Sun, W.; Zhong, Z. W.; Liu, J. W.; Gao, Q. S.; Hu, R. Z.; Zhu, M. *J. Power Sources* **2016,** *306*, 78-84.

(19) Lin, H.; Liu, N.; Shi, Z.; Guo, Y.; Tang, Y.; Gao, Q. *Adv. Funct. Mater.* **2016,** *26*, 5590-5598.

(20) Song, K.; Cho, E.; Kang, Y. M. *ACS Catal.* **2015,** *5*, 5116–5122.

(21) Bao, J.; Zhang, X.; Fan, B.; Zhang, J.; Zhou, M.; Yang, W.; Hu, X.; Wang, H.; Pan, B.; Xie, Y. *Angew.Chem. Int. Ed.*. **2015,** *54*, 7399-7404.

(22) Gao, R.; Li, Z.; Zhang, X.; Zhang, J.; Hu, Z.; Liu, X. *ACS Catal.* **2016,** *6*, 400-406.

(23) Gao, S.; Jiao, X.; Sun, Z.; Zhang, W.; Sun, Y.; Wang, C.; Hu, Q.; Zu, X.; Yang, F.; Yang, S.; Liang, L.; Wu, J.; Xie, Y. *Angew. Chem. Int. Ed.* **2016,** *55*, 698-702.

(24) Xu, L.; Jiang, Q.; Xiao, Z.; Li, X.; Huo, J.; Wang, S.; Dai, L. *Angew.Chem. Int. Ed.* **2016,** *128*, 5363-5367.

(25) Chen, S.; Duan, J.; Vasileff, A.; Qiao, S. Z. *Angew.Chem. Int. Ed*. **2016,** *55*, 3804-3808.

(26) Sun, Y.; Gao, S.; Lei, F.; Liu, J.; Liang, L.; Xie, Y. *Chem. Sci.* **2014,** *5*, 3976-3982.

(27) Hong, J.; Jin, C.; Yuan, J.; Zhang, Z. *Adv. Mater*. **2017,** 29,1606434.

(28) Sun, Y.; Liu, Q.; Gao, S.; Cheng, H.; Lei, F.; Sun, Z.; Jiang, Y.; Su, H.; Wei, S.; Xie, Y. *Nat. Commun.* **2013,** *4*, 2899.

(29) Kuang, Y.; Feng, G.; Li, P.; Bi, Y.; Li, Y.; Sun, X. *Angew. Chem.* **2016,** *128, 703– 707*.

(30) Zeng, X.; Leng, L.; Liu, F.; Wang, G.; Dong, Y.; Du, L.; Liu, L.; Liao, S. *Electrochim. Acta* **2016,** *200*, 231-238.

(31) Du, R.; Chen, Z. J.; Cai, Q.; Fu, J. L.; Gong, Y.; Wu, Z. H. *Science China Physics, Mechanics & Astronomy* **2016,** *59*, 1-8.

(32) Du, R.; Cai, Q.; Chen, Z.; Gong, Y.; Liu, H.; Wu, Z. *Instrum Sci Technol* **2016,** *44*, 1-11.

(33) Storm, M. M.; Christensen, M. K.; Younesi, R.; Norby, P. *J. Phys. Chem. C*, **2016**, *120*, 21211–21217.

(34) Zhang, J.; Li, P.; Wang, Z.; Qiao, J.; Rooney, D.; Sun, W.; Sun, K. *J. Mater. Chem. A* **2014,** *3*, 1504-1510.

(35) Yu, T.; Zhu, Y. W.; Xu, X. J.; Shen, Z. X.; Chen, P.; Lim C., T.; Thong, L. T.- J.; Sow, C., H. *Adv. Mater.* **2005,** *17*, 1595-1599.

(36) Xu, J. J.; Chang, Z. W.; Wang, Y.; Liu, D. P.; Zhang, Y.; Zhang, X. B. *Adv. Mater.* **2016,** *28*, 9620-9628.

(37) Sahoo, R.; Pal, A.; Pal, T. *Chem. Commun.* **2016,** *47*, 13528-13542.

(38) Song, C.; Zhang, D.; Wang, B.; Cai, Z.; Yan, P.; Sun, Y.; Ye, K.; Cao, D.; Cheng, K.; Wang, G. *Nano Res.* **2016,** *9*, 1-12.

(39) Wu, F.; Zhang, X.; Zhao, T.; Chen, R.; Ye, Y.; Xie, M.; Li, L. *J. Mater. Chem. A* **2015,** *3*, 17620-17626.

(40) Lin, F.; Markus, I. M.; Nordlund, D.; Weng, T.-C.; Asta, M. D.; Xin, H. L.; Doeff, M. M. *Nat. Commun.* **2014,** *5*, 3529.

(41) Luo, K.; Roberts, M. R.; Hao, R.; Guerrini, N.; Pickup, D. M.; Liu, Y.-S.; Edström, K.; Guo, J.; Chadwick, A. V.; Duda, L. C.; Bruce, P. G. *Nat. Chem.* **2016,** *8*, 684-691.

(42) Ogasawara, Y.; Hibino, M.; Kobayashi, H.; Kudo, T.; Asakura, D.; Nanba, Y.; Hosono, E.; Nagamura, N.; Kitada, Y.; Honma, I. *J. Power Sources* **2015,** *287*, 220-225.

(43) Wang, J.; Zhou, J.; Hu, Y.; Regier, T. *Energ Environ Sci* **2013,** *6*, 926-934.

(44) Tuxen, A.; Carenco, S.; Chintapalli, M.; Chuang, C. H.; Escudero, C.; Pach, E.; Jiang, P.; Borondics, F.; Beberwyck, B.; Alivisatos, A. P. *J. Am. Chem. Soc.* **2013,** *135*, 2273-2278.

(45) Liu, T.; Leskes, M.; Yu, W.; Moore, A. J.; Zhou, L.; Bayley, P. M.; Kim, G.; Grey, C. P. *Science* **2015,** *350*, 530-533.

(46) Zhu, Y. G.; Jia, C.; Yang, J.; Pan, F.; Huang, Q.; Wang, Q. *Chem. Commun.* **2015,** *51*, 9451-9454.

(47) Wu, F.; Lee, J. T.; Nitta, N.; Kim, H.; Borodin, O.; Yushin, G. *Adv. Mater.* **2015,** *27*, 101-108.

(48) Peng, Z.; Freunberger, S. A.; Hardwick, L. J.; Chen, Y.; Vincent, G.; Fanny, B.; Petr, N.; Duncan, G.; Tarascon, J. M; Bruce, P. G. *Angew.Chem. Int. Ed.* **2011,** *123*, 6351-6355.

(49) Yuan, C.; Yang, L.; Hou, L.; Shen, L.; Zhang, X.; Lou, X. W. *Energy Environ. Sci.***, 2012,** *5*, 7883-7887.

(50) Kwak, W. J.; Hirshberg, D.; Sharon, D.; Afri, M.; Frimer, A. A.; Jung, H. G.; Aurbach, D.; Sun, Y. K. *Energy Environ. Sci.***, 2016,** *9*, 2334-2345.

(51) Wang, Y.; Zhang, Y.; Liu, Z.; Xie, C.; Feng, S.; Liu, D.; Shao, M.; Wang, S. *Angew.Chem. Int. Ed.* **2017,** *56,5867-5871*.